Fluctuations and critical phenomena in catalytic CO oxidation on nanoscale Pt facets

Yu. Suchorski,[1] J. Beben,[2] R. Imbihl,[1] E. W. James,[3,4] Da-Jiang Liu,[3] and J. W. Evans[3,4]
[1]*Institut für Physikalische Chemie und Elektrochemie Universität Hannover Callinstrasse 3-3a, D-30167 Hannover, Germany*
[2]*Institute of Experimental Physics, Wroclaw University, pl. Maxa Borna 9, PL50-204 Wroclaw, Poland*
[3]*Ames Laboratory, Iowa State University, Ames, Iowa 50010*
[4]*Department of Mathematics, Iowa State University, Ames, Iowa 50017*
(Received 28 August 2000; published 4 April 2001)

Local fluctuations and fluctuation-induced transitions in catalytic CO oxidation are studied with field electron microscopy on the (112) facets of a [100]-oriented Pt field emitter tip. The reaction is investigated in the bistable range close to the cusp point (critical point) that terminates the bistability range in p_{CO}, T-parameter space. The amplitude and the spatial coherence of the fluctuations increase on approaching the critical point. The fluctuations are spatially well correlated on each flat (112) facet, but their correlation decays rapidly across stepped regions that terminate the flat facets. On smaller (112) facets, an onset of fluctuation-induced transitions is observed earlier (i.e., further away from the critical point) than for larger (112) facets. The behavior of the reaction system near the cusp point appears to be similar to that of an equilibrium system near the critical point. The observed fluctuations are mimicked in a simple reaction model for CO oxidation on surfaces that incorporates both rapid diffusion of adsorbed CO, and superlattice ordering of adsorbed immobile oxygen. The steady states of the model exhibit a cusp bifurcation, from a regime of bistability to one of monostability. The fluctuations increase near this cusp point, as in experiment. This behavior is analyzed via kinetic Monte Carlo simulations and analytic procedures, focusing on the consequences for fluctuation-induced transitions.

DOI: 10.1103/PhysRevB.63.165417 PACS number(s): 82.65.+r, 68.37.Ef, 82.40.Bj

I. INTRODUCTION

A well-known problem in heterogeneous catalysis is the so-called *pressure and material gap*, i.e., the difference between single-crystal studies conducted in UHV and real catalysis operating with composite materials as catalysts under pressures $\approx 1-100$ bar.[1] One important aspect of the material gap problem is that the reactivity of the small metal particles (typically, a few nm in size), which are present on supported catalysts, differs from those of macroscopic single-crystal planes. The small metal particles exhibit facets with different orientations, and hence reactivities, coupled together via surface diffusion of mobile adsorbates. Complex dynamic behavior may therefore result.[2] Moreover, due to the small dimensions of the facets, which comprise typically only a few hundred to a few thousand surface atoms, reaction-induced fluctuations will become important.

We can consider a field emitter tip as a model system, which allows us to study certain aspects of a catalytic reaction on a supported catalyst. Here, we have a structurally heterogeneous surface consisting of differently oriented facets of nm dimensions. The surface can be characterized with atomic resolution by field-ion microscopy (FIM). With field-electron microscopy (FEM), we can study the dynamics of the reaction imaging the surface *in situ* with a resolution of ≈ 2 nm and, thus, investigate the behavior of fluctuations. Catalytic surface reactions such as the reduction of NO on Rh, or the oxidation of CO on Pt, have been studied with FEM[3–5] [and the effect of the imaging field (<5 V/nm) was shown to be negligible for reactions like catalytic CO oxidation[6]].

With catalytic CO oxidation on a Pt field emitter tip as a model system, reaction-induced fluctuations have been systematically studied in recent years.[7–9] We have shown that different crystallographic orientations have different fluctuation characteristics.[8] In the bistable range of the reaction, fluctuation-induced transitions between the two branches of the reaction can occur, as predicted by theory.[9,10] Within a single facet, the fluctuations are typically well correlated, but so far, no significant correlation between fluctuations on different facets has been detected. Given the very fast diffusion of adsorbed CO, this absence of long-range correlations is rather surprising. Evidently structural heterogeneities such as atomic steps must terminate the spatial correlation of the fluctuations, e.g., due to strongly reduced CO diffusion across steps or an enhanced reactivity at step sites.

One decisive factor for the spatial coherence, as well as for the amplitude of the fluctuations, is the proximity to the cusp point terminating the bistable range of the reaction. By analogy, with phase transitions in equilibrium systems, this cusp point has also been described as a critical point, but it remains to be demonstrated how far the analogy really holds. The main point of this paper is to investigate the behavior of the amplitude and of the spatial coherence of the fluctuations upon approaching this critical point. One should expect that close to the critical point, the spatial coherence increases, potentially leading to synchronized fluctuations over different orientations.

In a preceding study, we observed that fluctuation-induced transitions occurred in a spatially well-correlated fashion in the vicinity of (110) facets.[9] In our present study, we focus on well-defined (112) facets, which are structurally homogeneous and surrounded by atomic steps. The choice of this particular orientation was motivated by the observation that even quite close to the cusp point, neighboring regions did not exhibit correlated fluctuations. This means that the dynamics on the (112) facet are not complicated by additional strong coupling effects.

The observed fluctuations are mimicked in a simple reaction model for CO oxidation on surfaces that incorporates both rapid diffusion of adsorbed CO, and superlattice ordering of adsorbed immobile oxygen. We show that the steady states of our model also exhibit a cusp bifurcation, from a regime of bistability to one of monostability, which is akin to a critical point in equilibrium systems. We analyze the increase in fluctuations near this transition, using kinetic Monte Carlo simulations, as well as analytic procedures, and elucidate the consequences for fluctuation-induced transitions.

II. EXPERIMENTAL RESULTS

A. Experimental methods

In our experiments, we use the FIM/FEM apparatus as a flow reactor with a Pt field emitter tip as catalyst. The measurements were performed with a bakeable metal UHV system, containing a tip assembly that allowed operation in a temperature range from 78 to 900 K, a channel plate for intensification of FEM/FIM images, and a gas supply for rare (Ne, He) and reactive (CO, O_2) gases. The details of the apparatus, as well as the analysis of the video data, are described elsewhere.[7,11,12]

An atomically clean surface is prepared by field evaporation under visual control by FIM that provides atomic resolution (0.2–0.3 nm). Under reaction conditions, the surface is imaged with FEM with a resolution of ≈2 nm. The FEM images were recorded with a conventional (25 frames/s) charge-coupled device (CCD) video camera (and a HI8-video recorder) as well as with a cooled digital CCD camera that allowed 100 frames/s (*SensiCam*, PCO Computer Optics). Images from the conventional CCD camera and the digital camera were digitized with 8 and 12 bit resolution, respectively.

The video data were digitized inside a selected rectangular ''profile window'' corresponding to a $2\times16\,\mathrm{nm}^2$ area on the tip surface. The window was positioned using the atomic resolution of FIM images. The distances on the tip surface were estimated from the angular separation of poles in the FIM image and the tip curvature.[13] For one-dimensional intensity profiles, the intensity was integrated along the short vertical side of the window. With the digital CCD camera, the time resolution was increased by reducing the number of pixels. The intensity of four neighboring pixels was added up to one pixel (2×2 binning). The size of the resulting larger pixel corresponds to $0.8\times0.8\,\mathrm{nm},^2$ which is still below the spatial resolution of FEM. Local time series were obtained by integrating the intensity in a $2\times2\,\mathrm{nm}^2$ window.

B. Bifurcation diagram and fluctuation amplitude

Catalytic CO oxidation on Pt exhibits two stable kinetic branches that coexist in the bistable range: an active branch in which the surface is predominantly oxygen covered (such that CO can still adsorb and react) and an inactive branch on which a high-CO coverage inhibits O_2 adsorption, and hence, poisons the reaction.[14] At elevated temperatures, kinetic oscillations are observed. These have been studied on various macroscopic single-crystal planes,[15] and also found on Pt field emitter tips of different orientations.[4,6] At lower temperature, the reaction is bistable on the Pt tip, and it is on this the range that we entirely focus here.

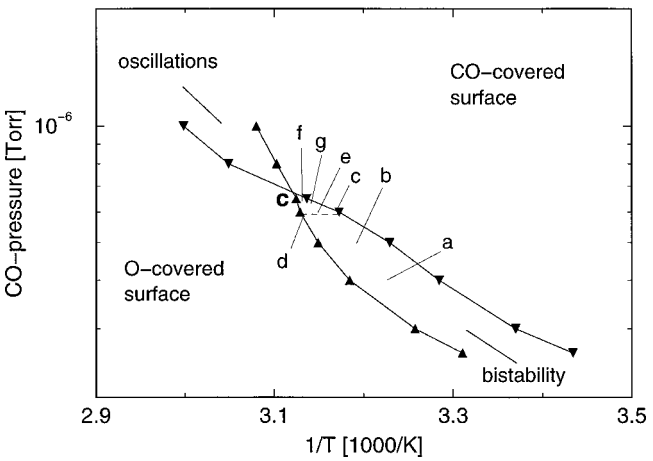

FIG. 1. Bifurcation diagram for catalytic CO oxidation on a [100]-oriented Pt tip at $P_{O_2}=4.0\times10^{-4}$ Torr as determined with FEM. Dashed lines indicate temperature scans, points $a-g$ correspond to particular time series. *C* denotes a cusp point terminating the bistability range.

The contrast in FEM is based mainly on the variation of the local work function. The Pt surface in its active state is oxygen covered and exhibits a high work function, corresponding to a low-FE M brightness. In its inactive CO-poisoned state, the surface exhibits a lower work function and appears bright in FEM. The corresponding bifurcation diagram (reactive phase diagram), showing the oscillatory and bistable range of the reaction (at constant $p_{O_2}=4.0\times10^{-4}$ Torr), is displayed in Fig. 1 for the particular [100]-oriented tip used here. Left of the bistable range, the system is in a stable oxygen-covered surface state, and to the right, the surface is in a stable CO-covered state. Upon cyclic parameter variation, a hysteresis in the state of the surface and in the reaction rate is observed. We note that the diagram in Fig. 1 refers to the whole imaged tip: at the lower boundary of the bistable range, the whole imaged surface undergoes simultaneously a fast transition (on the order of fractions of a second) from CO covered to an oxygen-covered state; at the upper boundary, it undergoes a slow transition (on the order of seconds) from an oxygen covered to a CO-covered state, respectively. The simultaneous appearance of the transitions on different facets is apparently a consequence of efficient coupling via fast CO diffusion.

Examples of time series showing fluctuations in the local FEM brightness on Pt (112) are displayed in Fig. 2. As indicated in Fig. 1, the time series have been recorded at points lying at various distances from the cusp point (critical point) that terminates the bistable range of the reaction. Time series *a*, *b*, *c*, *e*, *g* were taken with the system initially on the inactive branch, *d* and *f* on the reactive branch of the reaction.

The probability density distributions for the intensity amplitude of the time series have been included in the plots of Fig. 2. Particularly close to the critical point, they show pronounced deviations from a Gaussian-like distributions, which

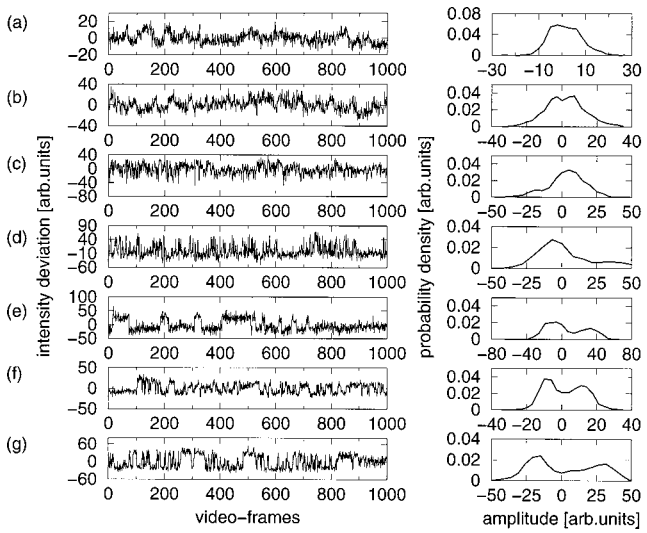

FIG. 2. Time series of the local FEM brightness monitored on a Pt (112) facet (left-hand side) and the resulting amplitude distributions (right-hand side). The data $a-g$ correspond to different points of the bistability region marked on the bifurcation diagram in Fig. 1.

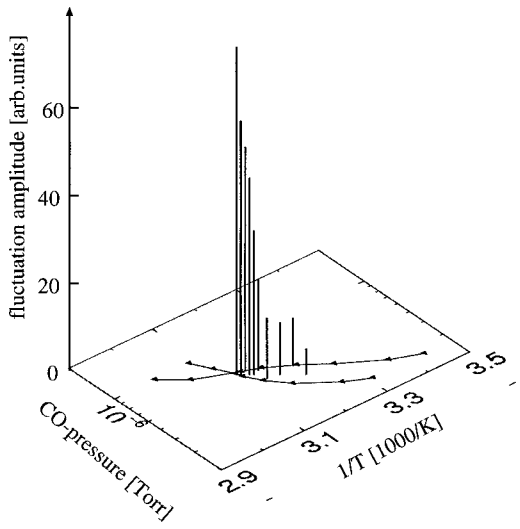

FIG. 3. Critical behavior of fluctuations in the vicinity of the cusp point *C*. Shown is average amplitude of local FEM brightness fluctuations of a spot of 2×2 nm size on Pt (112). The data refer to different points in the bistability range marked in the bifurcation diagram in Fig. 1.

characterize the monostable region of the reaction.[8,9] Previous studies have shown that inside the bistability region, the amplitude distribution broadens and becomes asymmetric. This has already been demonstrated for the (100), (111), and (113) facets (at $p_{CO}=4.0\times10^{-7}$ Torr, $p_{O_2}=4.0\times10^{-6}$ Torr).[8] As shown by Fig. 2, this is also valid for the (112) plane. We note that upon approaching the cusp point, the amplitude distribution becomes bimodal with first indications being already visible in curve *b* of Fig. 2 ($p_{CO}=5.0\times10^{-7}$ Torr). Within the bistability range, the amplitude distribution depends also on the position relative to the boundaries of the range. Closer to the critical point *C*, the bimodality becomes more pronounced and extends over a wider *T* range. Above the dashed line *c*-*d*, bimodal distributions are observed in the whole bistability range, but the distribution becomes strongly asymmetric towards the boundaries. Towards the low *T* boundary (right) the CO-covered state is more stable, and towards the high-*T* boundary (left) the oxygen-covered state is more stable. This is demonstrated by the asymmetries of the distributions in Figs. 2(c) and 2(d), where the temperature varies along the dashed line in Fig. 1.

Experimentally, one encounters a problem approaching the critical point because the system becomes increasingly unstable, probably as a result of reaction-induced restructuring of the tip, and tends to drift into a monostable state. This tendency became already apparent in the time series *c* and *d*. The parameter range in which the system was stable enough to record an approximately drift-free time series of at least 20 s duration extends up to $p_{CO}=6.5\times10^{-7}$ Torr, corresponding to *f*,*g*.

Figure 3 shows the variation of the amplitude of the fluctuations for different points in the bistability region. Displayed is the average amplitude of the local brightness fluctuations defined here as $\langle(i-\langle i\rangle^2)\rangle/\langle i\rangle$, where i is the local FEM brightness, and $\langle\,\rangle$ denotes an average over time. A drastic increase in the fluctuation amplitude close to the critical point is evident. A quantitative interpretation of the data in Fig. 3 should be considered with some care, due to the additional influence of the imaging process on the resulting FEM brightness. The field electron emission current depends exponentially on the local work function, but this dependence is convoluted by the local electric-field strength, which can vary depending on the local surface crystallography and on the adsorbate distribution. Earlier measurements of the local-field distribution over individual surface atoms conducted with field-ion appearance energy spectroscopy showed, however, that these local-field modifications are not strong enough to change the general trend visible in Fig. 3.[16,17]

C. Spatial coherence of the fluctuations

Fluctuations in a surface reaction exhibit spatial correlations due to diffusional coupling. Of particular interest here is the role of the atomic steps surrounding the (112) facet, since steps are known to exhibit a different reactivity and have a different bonding strength to adsorbates as compared to flat terrace regions.[18,19] Also, the discontinuous stop-and-go motion of reaction fronts in catalytic CO oxidation on a stepped Pt (100) surface has been attributed to a slowing down of CO diffusion across steps.[20] One should therefore expect that steps disturb the spatial coherence of fluctuations. Our earlier result that fluctuations on different facets are generally uncorrelated is in line with this expectation.

The spatial distribution of the fluctuation amplitude superimposed with a FIM image showing the surface topography is displayed in Fig. 4. The amplitude has its maximum in the center of the flat region and it decays away from it, rapidly reaching zero outside the steps surrounding the (112) facet. The amplitude distribution in Fig. 4(a) is more qualitative in nature because it also contains the dependence of the emission current on the surface crystallography. Spatial correla-

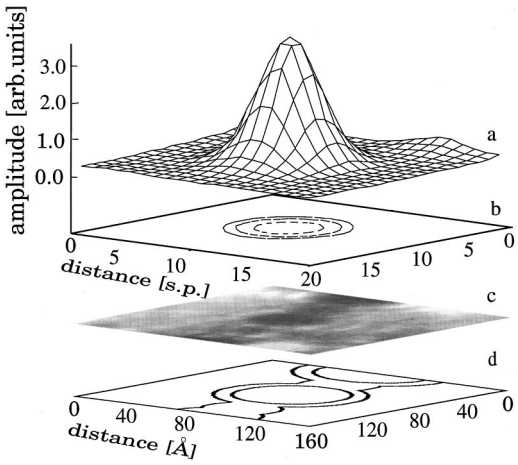

FIG. 4. Spatial distribution of the average amplitude of the fluctuations on Pt (112) facet during fluctuation-induced transitions (point *f* of the bifurcation diagram in Fig. 1). (a) Spatial distribution of the average amplitude of the fluctuations over the $16\times16\,\mathrm{nm}^2$ region shown in Fig. 4(c). The data correspond to the time series in Fig. 2(f). (b) Projection of (a) onto a plane. Indicated are lines of equal amplitude. The unit ''s. p.'' refers to ''superpixel:'' 1 s. p.$=0.8$ nm. (c) FIM image of the Pt (112) facet. (d) Schematic drawing of the crystallography of the region imaged with FIM in (c). The lines mark atomic steps.

tion functions were determined from local time series measured by integrating the FEM intensity inside two small square windows of $2\times2\,\mathrm{nm}^2$ size ($0.8\times0.8\,\mathrm{nm}^2$ for the digital camera). The spatial separation of the two windows was varied in such a way, that one of the window was kept fixed near the border of the (112) facet while the second window was moved across the facet. We obtain local time series for varying distances and can calculate the spatial (two-point) correlation functions as described elsewhere.[9,10]

Figure 5 shows in a linear-log plot, the spatial correlation functions for points *f,g,c* of the diagram in Fig. 1. The comparison of curves *f* and *g* with *c* demonstrates that the degree of spatial correlation increases towards the critical point. At the position marked by an arrow in Fig. 5, the (negative) slope of curves *f* and *g* increases strongly. To a smaller, but still clearly notable degree, this change in slopes is also visible for curve *c*. The comparison with the surface topography in the FIM image of Fig. 4(c) reveals that the change of the slopes coincides with the first atomic step at the edge of the facet. This indicates that atomic steps suffice to strongly reduce the spatial correlation of the fluctuations. It thus becomes plausible why no significant correlations between fluctuations on the (112) plane and on neighboring facets have been detected so far.

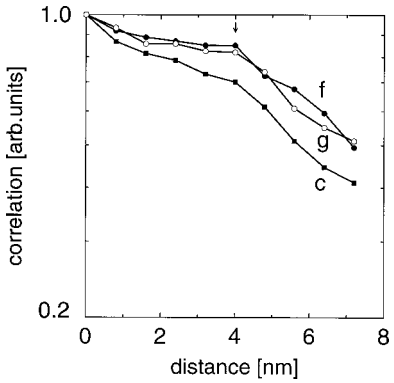

FIG. 5. Spatial (two-point) correlation of fluctuations on the (112) facet as determined from local ($0.8\times0.8\,\mathrm{nm}^2$) time series. The letters refer to the different time series shown in Fig. 2. The distance zero refers to the left edge of the facet.

It has been verified that the decrease of spatial correlation with increasing distance is not due to an increasing contribution of instrumental noise caused by the decaying amplitude of the fluctuations outside the (112) facet (see Fig. 4). Numerical simulations in which uncorrelated noise was superimposed on fluctuations with varying amplitude demonstrated that the increase in instrumental noise level can account at most for an estimated 20% reduction of spatial correlation for the largest distance in the diagram of Fig. 5.

The comparison with the time series in Fig. 2 shows that time series *f* and *g* exhibit a bimodal amplitude distribution which is the signature of noise-induced transition in a bistable system. As shown before, such noise-induced transitions are associated with a high degree of spatial coherence on a facet.[21] On the (112) facet, a rather perfect spatial coherence of the fluctuations is reflected by the flat part of curves *f* and *g* left of the arrow in Fig. 5.

A method that utilizes the full spatiotemporal information contained in the video images is POD, also known as *Karhunen-Loeve* (KL) *decomposition*.[22,23] This method has recently been applied to the analysis of FEM images showing reaction-induced fluctuations on a Pt tip.[21] Close to the critical point where the whole system becomes rather unstable, the KL method has the additional advantage that is also a method of noise reduction, thus allowing to use shorter image sequences.

For a spatiotemporal field, $w(x,t)$, the POD method yields an ''optimal'' basis of orthogonal functions (modes) $\Psi_n(x)$ which represent the signal (in our case, the fluctuations of the FEM image intensity) as

$$w(x,t)=\sum_{n=1}^{\infty}A_n(t)\Psi_n(x), \tag{1}$$

where $A_n(t)$ are the time-dependent amplitudes of the corresponding basis functions. The basis functions $\Psi_n(x)$ are the eigenfunctions of the equation

$$\hat{S}\psi_n(x)=\lambda_n\psi_n(x), \tag{2}$$

with eigenvalues λ_n and correlation matrix $\hat{S}$, with $S_{ij}=\langle w(x_i,t)w(x_j,t)\rangle_t$, representing the two-point correlation function, where x_i and x_j are the image pixels and $\langle\,\rangle_t$, means time average. Each mode captures a percentage of the overall dataset content (energy in a mean-square sense) quantified by the corresponding eigenvalue, λ_n. In cases where the spatiotemporal dynamic behavior is governed by only a few degrees of freedom, the first few modes are seen to contain most of the energy (most of the signal content),

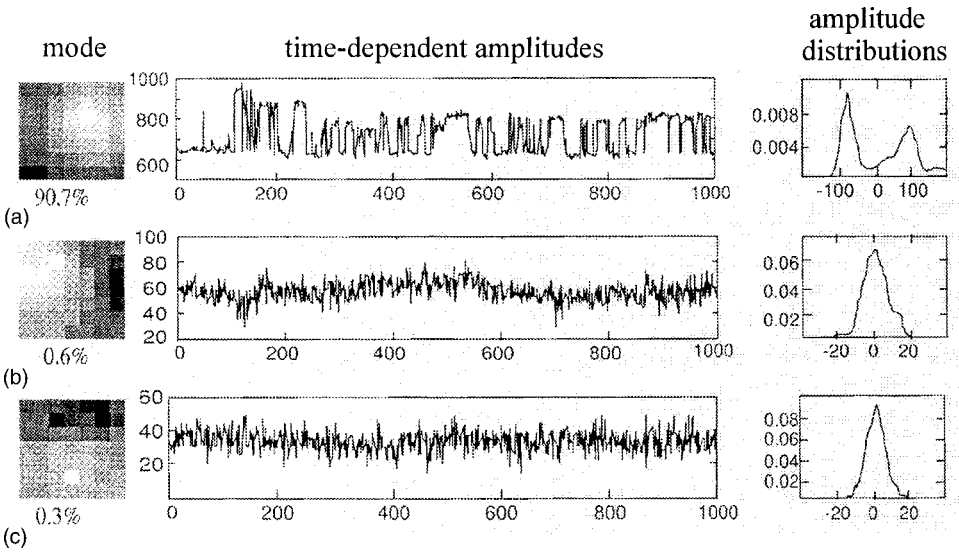

FIG. 6. (a)–(c) Results of a POD analysis for fluctuations on the reactive branch in the bistable region (point *f* in Fig. 1). Shown are the first three POD modes, the time-dependent amplitudes, the energy values, and the amplitude distributions. A video sequence of 1000 frames was analyzed using a window of $5.6\times5.6\,\mathrm{nm}^2$ with a 7×7 grid of pixels. The region from which the data were taken is in the center of the (112) facet shown in the Fig. 4(c).

and have high eigenvalues (weights), while the remaining modes and coefficients are negligible.

Figure 6 shows the results of a POD analysis of a video-sequence taken at point *f* in the bifurcation diagram (Fig. 1). The size of the analyzed area was chosen as $5.6\times5.6\,\mathrm{nm}^2$, which is roughly equal to the diameter of the (112) facet. Figures 6(a)–6(c) show the first three spatial modes (eigenfunctions) and the corresponding time-dependent amplitudes. In addition, the probability distributions are displayed that have been computed from the time-dependent amplitudes. The first mode [Fig. 6(a)] captures already 90% of the total energy of the modes and the higher modes contribute only marginally. The presence of one dominating mode reflects the high degree of spatial coherence of fluctuations in agreement with the correlation analysis of the time series (Fig. 5, curve *f*), where the spatial correlation decreases to no more than 80% of its maximum value within the flat (112) surface. The effect of noise reduction is visible in the probability distribution of the first mode in Fig. 6, which exhibits a more pronounced bimodal distribution, as compared to the corresponding time series in Fig. 2(f).

The amount of computation for a POD analysis can be reduced significantly by using ''quasi-1D images'' taken from the 2×16 nm profile window. Such a ''one-dimensional'' POD analysis was conducted for video sequences corresponding to time series $a-g$ in Fig. 2. The results summarized in Fig. 7 show that the energy values captured by the first mode increase significantly towards the critical point. Close to the critical point, the first mode captures over 90% of the total fluctuation energy indicating spatially coherent fluctuations on the (112) facet. Similar behavior is well known for the equilibrium systems near the critical point where the correlation length diverges (in an infinite system).[24] In our case, the correlation length appears to be limited by the size of the facet. Both the amplitude of the fluctuations and the degree of spatial coherence increase simultaneously towards the critical point.

Due to spatial coupling and boundary effects, the system size should play an important role for fluctuations. Our [100]-oriented tip exhibits four well-observable (112) facets with diameters 4.5, 5.0, 5.5, and 6.0 nm. Generally, the fluctuation behavior was quite similar for all sized facets. However, we note that for the smallest (4.5 nm) facet, the onset of the fluctuation-induced transitions occurs ''earlier,'' i.e., further away from the critical point (below point *b* in Fig. 1), than for the larger facets, where the distribution became bimodal only slightly above point *b*.

III. THEORETICAL MODELING

There is a considerable body of theoretical (and experimental) work examining the effect of noise on systems displaying nonlinear dynamics. It is particularly appropriate here to mention previous studies of transitions in bistable systems described by simple potential models,[25,26] and of fluctuations in homogeneous chemical reactions,[27] where in both cases, stochastic behavior is induced by *external* noise. However, for the type of surface reactions of interest here, fluctuations are due to *internal* noise resulting from the stochastic nature of adsorption, desorption, reaction, and diffusion. Fortunately, such internal noise can, in principle, be

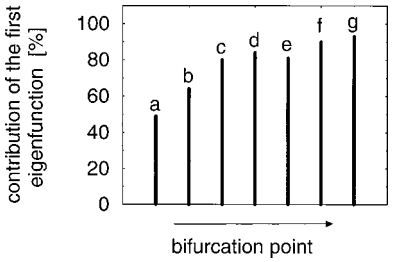

FIG. 7. Schematic diagram showing an increasing degree of spatial coherence for fluctuations close to the cusp point *C* (see Fig. 1). The energy values (in percent of the total energy) of the first POD mode are presented. The different points $a-g$ refer to the bifurcation diagram in Fig. 1. For part of the video sequences $(a-d,g)$ a one-dimensional POD analysis with a 2 nm-wide window across the (112) plane was used; for time series *e* and *f* a 2D-POD analysis with $5.6\times5.6\,\mathrm{nm}^2$ square window was conducted. The windows were placed in the center of the (112) plane.

naturally and correctly incorporated into atomistic lattice-gas (LG) models for surface reactions. We note one previous LG study, which examined a noise-induced transition to bistability for an idealized, deterministically monostable surface reaction model.[10] However, to describe the experimental observations outlined above, we need a realistic model for CO oxidation. Such a model must account for the effect of rapid CO diffusion in quenching fluctuations,[28,29] for the compensating feature that adspecies interactions induce spatial ordering,[30] and for the additional feature that critical behavior at cusp bifurcations enhances fluctuations.[9] Most previous LG modeling of CO oxidation was based upon simplified ZGB (Ziff-Gulari-Barshad) type models,[31] which do not incorporate all of these features.

A. Model for CO oxidation and the ''hybrid'' simulation procedure

We consider a LG model for CO oxidation on surfaces represented as an $L\times L$ square grid of adsorption sites with periodic boundary conditions. The model incorporates the following steps:[9]

(i) CO (gas) adsorbs onto single empty sites at rate p_{CO}. CO (ads) hops very rapidly to nearby empty sites on the surface, and also desorbs from the surface at rate d.

(ii) O_2 (gas) adsorbs dissociatively at diagonal nearest-neighbor (NN) empty sites, *provided* that the *additional* six sites adjacent to these are not occupied by O (ads). This ''8-site rule'' [32] reflects ''infinite'' NN O (ads)-O (ads) repulsions. The impingement rate is p_{O2}. O (ads) is also immobile and cannot desorb. These rules ensure that O (ads) never occupies adjacent sites.

(iii) Each adjacent pair of CO (ads) and O (ads) reacts at rate k to form CO_2 (gas).

Our model is still simplistic. We neglect CO (ads)-O (ads) and CO (ads)-CO (ads) interactions, and also assume common adsorption sites for CO (ads) and O (ads) (with a maximum occupancy of unity). However, the O (ads)-O (ads) interactions produce commonly observed superlattice ordering [in this case, $c(2\times 2)$ ordering] of O (ads),[30,32] and eliminate artificial ZGB-type O poisoning.[30] Desorption is included in our model since, although the experimental temperature is low compared to single-crystal studies, the activation barrier for desorption is likely reduced as a result of higher surface coverages (due in turn to slower reaction).[33] The model does not support oscillatory kinetics (which requires additional feedback in the reaction mechanism), but it is only applied to describe experimental behavior in the bistable region. This and related models have been discussed previously in Refs. 9,34–36

Explicit results for our model will be reported only for the regime of infinitely mobile CO (ads). Here, the lack of interaction between CO (ads) and other CO (ads) or O (ads) implies that CO (ads) is *randomly distributed* (at each time) on sites not occupied by O (ads). We thus adopt a ''hybrid'' simulation approach:[28] we track only the total number, N_{CO} of CO (ads) in the system, but describe the distribution of O (ads) by a full lattice-gas simulation. The latter provides in particular the number, N_{O}, of O (ads). Our simulation of adlayer evolution assigns a mean-field-type probability, $N_{\mathrm{CO}}/(L^2-N_{\mathrm{O}})$, that any non-O (ads) site is occupied by CO (ads). We emphasize that the coverages, $\theta_J=N_J/L^2$, for $J=$CO or O, are instantaneous values that fluctuate in time, even in reactive or inactive steady states. We will use the notation $\langle\theta_J\rangle$ to denote the ergodic or time averages of these quantities. Finally, for this model, we mention that O (ads) interior to and on the perimeter of $c(2\times 2)$-O (ads) domains are equally reactive (cf. Ref. 37), and correspondingly the total reaction rate is given *exactly* by $4k\theta_{\mathrm{CO}}/\theta_{\mathrm{O}}(1-\theta_{\mathrm{O}})$.[35]

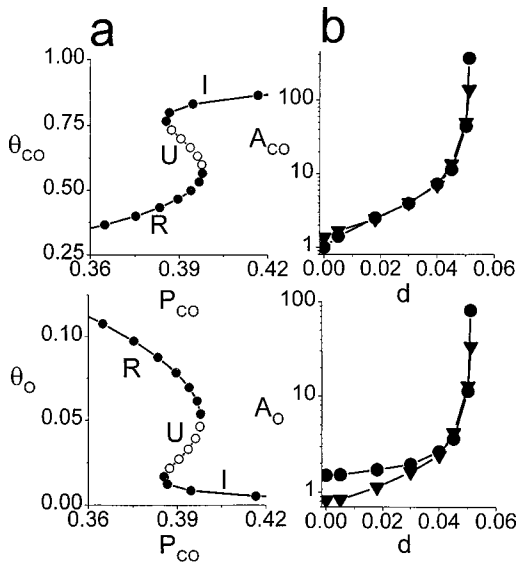

FIG. 8. (a) p_{CO} dependence of the coverages for the stable reactive (R) and inactive (I) steady states (solid circles), and for the unstable (U) steady state (open circles), when $d=0.040$; (b) Normalized amplitudes $A_J=L^2\langle\delta\theta_J^2\rangle/[\langle\theta_J\rangle(1-\langle\theta_J\rangle)]$, of coverage fluctuations for species $J=$CO and O. Data is taken at the midpoint of the bistable region for $d<d_c$, and for $L=150$. In (b), the circles (inverted triangles) refer to the inactive (reactive) steady states.

B. Bifurcation diagram, fluctuations, and correlations in a large system

In this subsection, we briefly sketch the behavior of our model for large systems, setting $p_{\mathrm{CO}}+p_{\mathrm{O2}}=k=1$. The model supports bistability for sufficiently low d, i.e., for a range of the parameter p_{CO}, a stable reactive state (with low θ_{CO} and high θ_{O}) coexists with a relatively inactive state (with high θ_{CO} and low θ_{O}). The bistable region ranges from $p_{\mathrm{CO}}=0$ to $p_{\mathrm{CO}}=0.360$ when $d=0$, and its width decreases with increasing d, vanishing at a critical value of $d_c\approx 0.053$ (and $p_{\mathrm{CO}}=0.414$), which corresponds to a cusp bifurcation point. Figure 3(a) in Ref. 9 shows the bifurcation diagram in the (p_{CO},d) plane. Figure 8(a) indicates the dependence on p_{CO} of the coverages for both stable steady states, and for a ''connecting'' unstable state, for $d=0.040$ where the bistable region ranges from $p_{\mathrm{CO}}=0.387$ to $p_{\mathrm{CO}}=0.398$. We will consider this case in more detail below.

Next, we consider behavior approaching the cusp bifurcation (or critical) point, always selecting p_{CO} to correspond to the midpoint of the bistable region. Analysis of time series

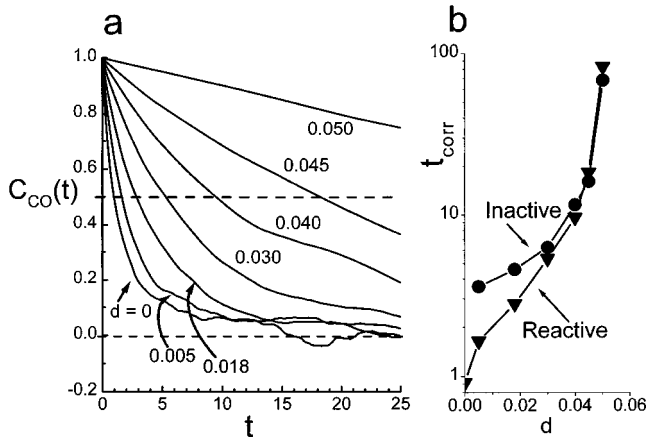

FIG. 9. (a) $C_{CO}(t)$ versus t for the reactive steady state at the midpoint of the bistable region, and for various d (shown); (b) the corresponding increase in t_{corr}, for inactive and reactive branches as $d \to d_c$.

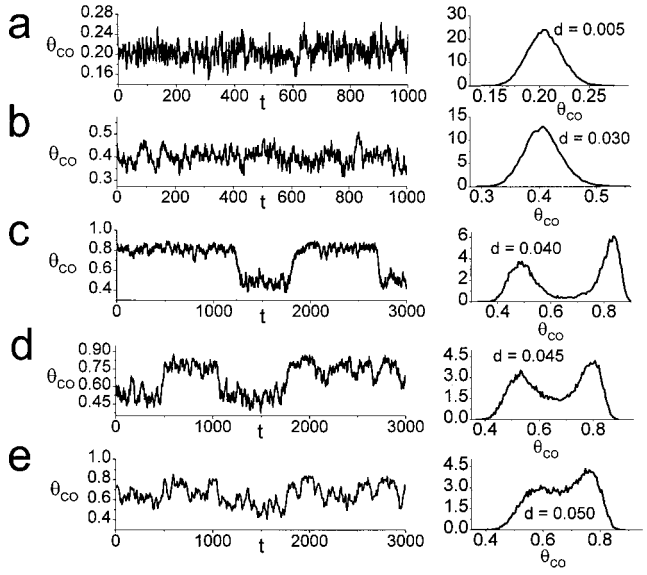

FIG. 10. (a)–(e). Time series for θ_{CO} at the midpoint of the bistable region for various d (shown) approaching d_c. The associated probability distributions, $P(\theta_{CO})$, were obtained from data for longer time series where the system started in the reactive state (see the text). Here $L=30$.

for the coverage fluctuations, $\delta\theta_J = \theta_J - \langle\theta_J\rangle$, reveals that their root-mean-square (RMS) amplitudes increase as $d \to d_c$ (from below). In Fig. 8(b), we plot the normalized amplitudes $A_J = L^2\langle\delta\theta_J^2\rangle/[\langle\theta_J\rangle(1-\langle\theta_J\rangle)]$, for $J=$CO and O. The observed increase in the A_J approaching the cusp bifurcation point is a direct analogue of the increase of fluctuations (''critical opalescence'') near a thermodynamic critical point.[24] The relationship of this behavior to an increase in some measure of spatial correlation length, and insight into other aspects of A_J behavior, comes from the application of fluctuation-correlation relations (see Appendix A). We also note that $\delta\theta_{CO}$ is anticorrelated with $\delta\theta_O$ (when $\delta\theta_{CO}$ increases, $\delta\theta_O$ tends to decrease), a feature that might be anticipated from the general fluctuation-correlation relations in Appendix A. Quantitatively, for the reactive state in the midpoint of the bistable region, the correlation factor, $\langle\delta\theta_{CO}\delta\theta_O\rangle/(\langle\delta\theta_{CO}^2\rangle^{1/2}\langle\delta\theta_O^2\rangle^{1/2})$, varies from about $-1/2$ to -1, as d increases from 0 toward d_c.

It is also instructive to assess temporal correlations in the coverages, as measured via

$$C_J(t) = \langle\delta\theta_J(t+t_0)\delta\theta_J(t_0)\rangle/\langle\delta\theta_J^2\rangle, \quad \text{for } J=\text{CO or O}. \tag{3}$$

These autocorrelations decrease monotonically from unity with increasing t. We can simply, but somewhat arbitrarily, define a correlation time, t_{corr}, to satisfy $C_J(t_{corr})=1/2$. Figure 9(a) shows the behavior of $C_{CO}(t)$ versus t, approaching the critical point as above. Clearly, the rate of decay slows closer to d_c, corresponding to an increase in t_{corr}, as shown in Fig. 9(b).

The above behavior is also analogous to that at a thermodynamic critical point.[24] In particular, the increase in t_{corr} mimics ''critical slowing down.'' This can also be understood within the context of nonlinear reaction kinetics: t_{corr} scales like the inverse of the smallest eigenvalue, λ_{min} of the linearized decay modes for the reaction kinetics,[26] and in general, one has that $\lambda_{min} \to 0$, approaching a cusp bifurcation point (i.e., as $d \to d_c$). It is also possible to show from the master equations for our reaction model that this increase in correlation time induces an increase in spatial correlation. A detailed discussion will be presented elsewhere.

C. Fluctuation-induced transitions in small systems

Since the RMS amplitudes of coverage fluctuations scale inversely with linear system size (see Appendix A), the fluctuations described above are not sufficient to induce transitions between the stable steady states for large systems. Thus, one has true bistability on extended single-crystal surfaces. In contrast, fluctuation-induced transitions are possible for small systems, as seen in the experimental observations for the ~6.0 nm diameter Pt (112) facet. This motivates us to examine model behavior for a similarly sized ''small'' 30×30 site lattice (where we use periodic boundary conditions). To this end, we examine the time series for θ_{CO}, thereby extracting the associated probability distribution $P(\theta_{CO})$, which we normalize so that $\int dx\, P(x)=1$. Similar results (not shown) were obtained from times series for θ_O. The units of time shown below correspond to again setting $p_{CO}+p_{O_2}=k=1$.

Figure 10 shows a sequence of time series for θ_{CO} taken choosing p_{CO} at the midpoint of the bistable region, for various d (shown) approaching the critical value of $d_c \approx 0.053$. For small d below about 0.04, the amplitude of the fluctuations is insufficient to induce transitions from the reactive to the inactive branch over the observation time of 30 000 time units. The $P(\theta_{CO})$ with the system starting in the reactive state (and taken from data over 30,000 time units) are monomodal, peaked about the mean coverage for the reactive branch. See Figs. 10(a) and 10(b). For $d \approx 0.040$, infrequent transitions between branches occur. Since the amplitude of the fluctuations about each branch is small compared with

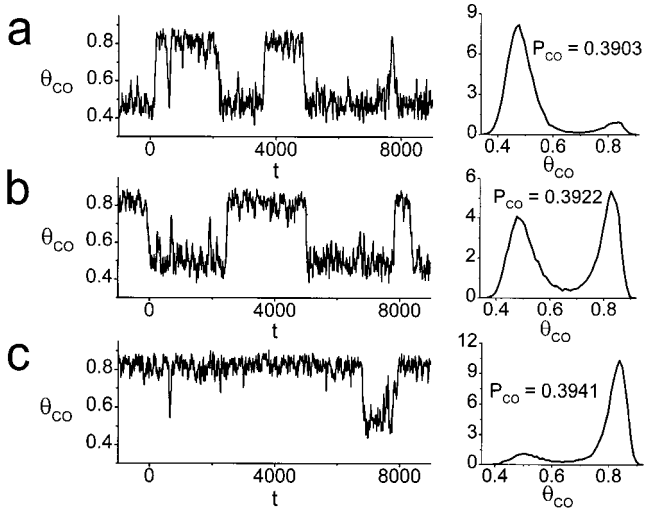

FIG. 11. (a)–(c). Time series for θ_{CO} and associated probability distributions, $P(\theta_{CO})$, for fixed $d=0.040$, and various p_{CO} (shown) scanning the bistable region $0.3866<p_{CO}<0.3978$. Here $L=30$.

the ''distance'' between them, $P(\theta_{CO})$ (again taken over 30 000 time units) adopts a well-defined bimodal form with peaks at the mean coverages for both steady state branches. See Fig. 10(c). Closer to the critical point, transitions between branches become more frequent, and the amplitude of the fluctuations about each branch become larger, eventually smearing the bimodal form of $P(\theta_{CO})$. See Fig. 10(d) [Fig. 10(e)] for $d=0.045$ ($d=0.050$). This simulated sequence of time series should be compared with the experimental subsequence in Figs. 2(a), 2(b), 2(e), 2(g), 2(f).

Figure 11 shows a sequence of time series for θ_{CO} at fixed $d=0.040$, scanning the bistable region by varying p_{CO} between the lower saddle-node bifurcation (or spinodal) at $p_{CO}=0.3866$, and the upper spinodal at $p_{CO}=0.3978$. This roughly corresponds to maintaining a fixed distance from the critical point. The corresponding $P(\theta_{CO})$ (from data over 30,000 time units) reflect behavior apparent in the time series: the system mainly resides in the more stable reactive state (with low θ_{CO}) for smaller p_{CO}, and in the more stable inactive state (with high θ_{CO}) for higher p_{CO}. The ''equistability point,'' where the system spends an equal amount of time in both states, is close to the midpoint of the bistable region. The simulated time series for fixed $d=0.04$ should be compared with the experimental subsequence in Figs. 2(d), 2(e), 2(c). The above type of equistability criterion naturally applies for finite systems with linear dimensions much smaller than the surface diffusion length. A different type of ''inhomogeneous equistability criterion,'' for spatially extended bistable surface reaction systems, is formulated in terms of the propagation of the chemical wave front separating the two states over a macroscopic length scale controlled by diffusion of CO (ads).[38]

The key aspects of fluctuation behavior described above are seen in the experiments. The main feature is that fluctuation-induced transitions between the bistable states become possible and increasingly prevalent closer to the critical point d_c as the amplitude of the fluctuations increases. In addition, one can use the model to explore the dependence of the onset of fluctuation-induced transitions on system size, just as was done in experiment. As expected, one finds this onset is delayed for larger sizes, e.g., shifting from $d\approx 0.040$ for a 30×30 site system to $d\approx 0.045$ for a 60×60 site system. Of course, these onset d's depend on the observation time (as a system will eventually jump between branches for any $d>0$), but the above onsets are quite robust for observation times on the order of tens of thousands of time units.

D. Population dynamics formulation for fluctuations in the hybrid reaction model

While the above KMC simulations can provide a precise characterization of fluctuation behavior in our reaction model, they constitute to some extent a ''black box'' providing somewhat limited insight into the underlying causes. For this reason, it is instructive to develop simpler (albeit approximate) analytic formulations of fluctuation behavior. These help clarify, e.g., which are the essential features behind the increase in fluctuations at the cusp bifurcation point.

To this end, we consider mean-field-type chemical kinetics treatments of *finite* reaction systems, where one describes the ''birth-death dynamics'' of the discrete numbers (or populations) of various reactant species by developing master equations for the associated population probability distributions.[39] These probability distributions contain infor-

TABLE I. Processes, population changes, and rates for our rate equation treatment of the dynamics of N_{CO} and N_O for an $L\times L$ site system. S denotes the O_2 sticking probability of finding a suitable ensemble of eight sites *not* occupied by O (ads) [denoted by P_8], of which the central two are also empty [conditional probability Q]. Since CO (ads) are randomly distributed, one has that $Q=(L^2-N_{CO}-N_O)/(L^2-N_O)\times(L^2-1-N_{CO}-N_O)/(L^2-1-N_O)$. The left factor equals the probability that the first non-O (ads) site is empty, and the right factor, that the second is empty (given that since the first site is empty, the N_O adsorbed O are known to be distributed on the remaining L^2-1 sites).

Process	Population Change	Rate
CO adsorption	$(N_{CO},N_O)\rightarrow(N_{CO}+1,N_O)$	$W_{COads}(N_{CO},N_O)=p_{CO}(L^2-N_{CO}-N_O)$
CO desorption	$(N_{CO},N_O)\rightarrow(N_{CO}-1,N_O)$	$W_{COdes}(N_{CO},N_O)=d\,N_{CO}$
CO+O reaction	$(N_{CO},N_O)\rightarrow(N_{CO}-1,N_O-1)$	$W_{react}(N_{CO},N_O)=4k\,N_O\cdot N_{CO}/(L^2-N_O)$
O_2 adsorption	$(N_{CO},N_O)\rightarrow(N_{CO},N_O+2)$	$W_{O2ads}(N_{CO},N_O)=p_{O2}L^2S\equiv p_{O2}L^2QP_8$

mation about fluctuations in particle numbers. In the regime of large particle numbers, these equations may be recast in the form of a generalized Fokker-Planck equation. It is natural to refine this approach to treat our surface reaction model, and to assess the extent to which it captures actual fluctuation behavior. One advantage in implementing this treatment for our model is that not just the rates for adsorption and desorption of CO, but also that for reaction (cf. Sec. III A), can be described exactly in terms of particle numbers. However, the rate for dissociative adsorption of oxygen depends on the details of the $c(2\times2)$-O (ads) ordering, so some approximation is required in its description.[35]

Specifically, our treatment tracks only the numbers $N_{CO} \leq L^2$ of CO (ads), and $N_O \leq L^2/2$ of O (ads), in the $L \times L$ site system. These numbers change stochastically due to the adsorption, desorption, and reaction processes in the manner indicated in Table I. The transition rates also listed in Table I are self-evident for CO adsorption and desorption. The rate for reaction accounts for the probability, $N_{CO}/(L^2 - N_O)$, that each site adjacent to an O (ads) is occupied by CO (ads). Only the rate for O_2-adsorption involves a nontrivial factor P_x, which gives the probability of finding a suitable ''adsorption ensemble'' of eight sites *not* occupied by O (ads) (see Appendix B). It is now straightforward to write down the master equations for the (normalized) probability, $P(N_{CO},N_O)$, for various particle populations as

$$\begin{aligned} d/dt\, P(N_{CO},N_O) = {} & W_{COads}(N_{CO}-1,N_O)P(N_{CO}-1,N_O) - W_{COads}(N_{CO},N_O)P(N_{CO},N_O) \\ & + W_{COdes}(N_{CO}+1,N_O)P(N_{CO}+1,N_O) - W_{COdes}(N_{CO},N_O)P(N_{CO},N_O) \\ & + W_{O2ads}(N_{CO},N_O-2)P(N_{CO},N_O-2) - W_{O2ads}(N_{CO},N_O)P(N_{CO},N_O) \\ & + W_{react}(N_{CO}+1,N_O+1)P(N_{CO}+1,N_O+1) - W_{react}(N_{CO},N_O)P(N_{CO},N_O). \end{aligned} \tag{4}$$

Integration of these $\sim L^4/2$ coupled equations provides the evolution of the probability distribution from any prescribed initial distribution. Then, reduced distributions such as $P(N_{CO}) = \Sigma_{NO} P(N_{CO},N_O)$ can be compared with $P(\theta_{CO} = N_{CO}/L^2)$ obtained from simulations in Sec. III C.

For an analysis of time evolution of the system (4), it is often more convenient to directly simulate the stochastic time series $\{N_{CO}(t),N_O(t)\}$: at each Monte Carlo simulation step, one changes the values of N_{CO} and N_O in one of the four ways indicated in Table I chosen with probabilities proportional to the associated rates. In addition, one must account for the varying residence times for different states $\{N_{CO},N_O\}$, which are given by the inverse of the total transition rate out of that state. Figure 12 shows results from this

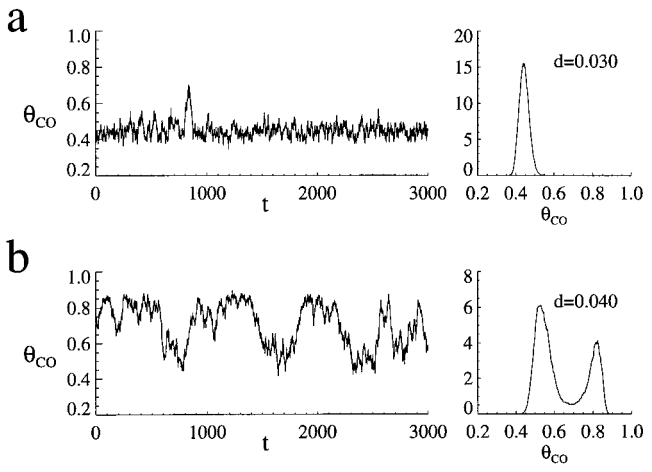

FIG. 12. Results corresponding to Fig. 10 from population dynamics simulations for: (a) $d=0.030$; and (b) $d=0.040$. Here $L=30$.

treatment that reproduces a transition seen in Sec. III C from monomodal to bimodal probability distributions at the midpoint of the bistability region, as increasing d from 0.030 to 0.040 (and using data over 30 000 time units). The rate of transitions between steady-state branches at $d=0.040$ in Fig. 12(b) appears to be higher than in the full simulations [cf. Fig. 10(c)]. However, this may reflect the lower critical $d_c = 0.048$ (compared with the exact $d_c = 0.053$) predicted by this approximate treatment.[35]

Finally, we note that ''true'' steady-state probability distributions (for infinite observation time) can be obtained from a direct analysis of the time-invariant solutions of the master equations (4). These distributions are always bimodal in the bistable region, as the system will eventually make transitions between the steady-state branches. (See Fig. 13.) The well-separated bimodal peaks for $d=0.030$ (in contrast to $d=0.040$) is consistent with very infrequent transitions between branches in the former case.

E. Further discussion

As indicated above, our simplistic model for CO oxidation captures many of the qualitative features of the fluctuation behavior observed in experiment. However, further model refinement will undoubtedly be necessary for a more quantitative comparison, particularly with spatial aspects of observed behavior. It is clear that our *neglect* of significant adspecies interactions, such as CO (ads)-O (ads) repulsions [which exist in addition to the very strong O (ads)-O (ads) NN repulsion], will artificially *limit* spatial correlations or coherence in the model. Furthermore, in reality, one expects O (ads) on the perimeter of ordered domains will have different reactivity from those in the interior (contrasting our model). This would introduce an additional spatial aspect to the reaction dynamics that could influence the nature of tran-

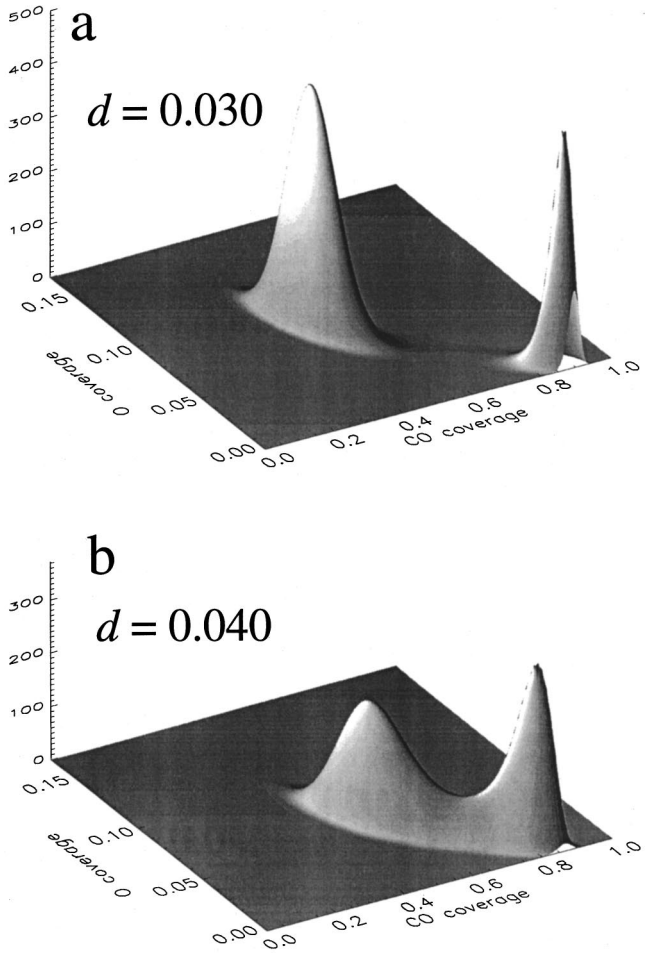

FIG. 13. Steady-state probability distributions from direct analysis of the time-invariant solutions of the master equations at the midpoint of the bistable region for: (a) $d=0.030$; and (b) $d=0.040$. Note that the bistable region in the mean-field treatment is shifted slightly from its exact location, as is d_c. Here $L=30$.

sitions between the steady-state branches. For these reasons, we do not compare model behavior for spatial correlations and POD modes with experiment, but will pursue these issues with a refined model.

IV. CONCLUSIONS

We have demonstrated that the reaction-induced fluctuations which occur in catalytic CO oxidation on small (112) facets of a Pt field emitter tip behave, in many respects, rather similarly to the fluctuations in an equilibrium system near a critical point. Upon approaching the critical point of the bistability range, the amplitude of the fluctuations and their spatial coherence increases strongly. Close to the critical point, the spatial correlations decay by less than 20% over the whole (112) facet, but they decays rapidly in the stepped regions terminating the (112) facet. A hybrid lattice-gas reaction model for CO oxidation on small Pt patches was presented, and shown to reproduce the essential features of the experiment.

ACKNOWLEDGMENTS

The experimental part of the work was supported by the Deutsche Forschungsgemeinschaft, J.B. acknowledges also the travel grant from the Deutsche Forschungsgemeinschaft. E.W.J., D.J.L., and J.W.E. were supported by the Division of Chemical Sciences, Office of Basic Energy Sciences, of the U.S. Department of Energy (USDOE). Work was performed at Ames Laboratory, which is operated for the USDOE by Iowa State University under Contract No. W-7405-Eng-82.

APPENDIX A: FLUCTUATION-CORRELATION RELATIONS

Let the occupation number $n_r^J=1$ if site r is occupied by species J, and $n_r^J=0$ otherwise (so $N_J=\Sigma_r n_r^J$ and $\theta_J=N_J/L^2$). We consider time averages, $\langle\,\rangle$, taken over either a finite or infinite observation time. We define the pair correlation for species J to be on site r, and K to be on r', as

$$C_{JK}(r,r')=\langle n_r^J n_r^K\rangle-\langle n_r^J\rangle\langle n_r^K\rangle. \tag{A1}$$

For finite systems with periodic boundary conditions (PBC), $C_{JK}(r,r')=C_{JK}(r-r')$, where $C_{JK}(0)=\langle\theta_J\rangle\delta_{J,K}-\langle\theta_J\rangle\langle\theta_K\rangle$. Using defining relation for θ_J, and setting $\delta\theta_J=\theta_J-\langle\theta_J\rangle$, one can show that

$$\langle\delta\theta_J\cdot\delta\theta_K\rangle=L^{-4}\sum_r\sum_{r'}C_{JK}(r,r')$$

$$\rightarrow L^{-2}\sum_K C_{JK}(x=r-r')\ \text{ for PBC.} \tag{A2}$$

For $J=K$, Eq. (A2) becomes $\langle\delta\theta_J^2\rangle=L^{-2}\Sigma_x C_{JJ}(x)$, relating coverage fluctuations to spatial correlations. In an infinite random system, only the lead $x=0$ term on the right-hand side (RHS) of Eq. (A2), $\langle\theta_J\rangle(1-\langle\theta_J\rangle)$, is nonzero, motivating our normalization of the A_J. We can now elucidate the behavior of the A_J as $d\rightarrow 0$, for finite systems shown in Fig. 8(c). For the inactive state, as $d\rightarrow 0$, one has $A_{\mathrm{CO}}\rightarrow 1$ (the adlayer becomes random, and ultimately CO poi-

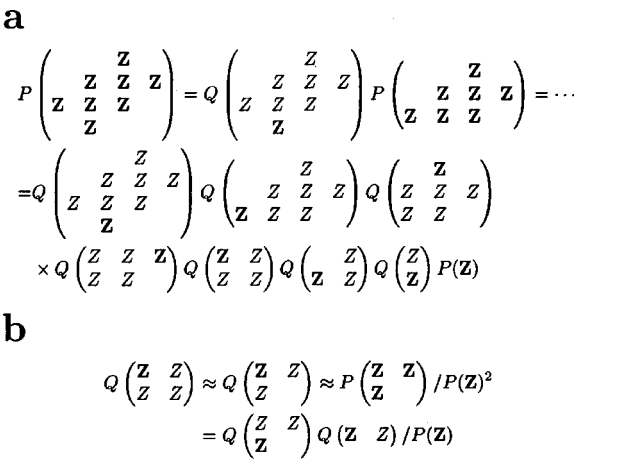

FIG. 14. Schematics of: (a) the factorization of P_8 in terms of conditional probabilities; (b) the further factorization of Q_3. Note that italic Z's represent sites specified to be in state **Z**.

soned), but $A_O \to 1.5$ (despite the feature that $\langle \theta_O \rangle \to 0$). The latter result follows recognizing that O (ads) dynamics in this regime consists of rare dimer adsorption events, followed by random removal of each of the constituent monomers (with an exponential waiting-time distribution) before another dimer adsorbs. Since the reactive state is nontrivial when $d \to 0$, one finds nontrivial limits for $A_{CO} > 1$, and $A_O < 1$ (reflecting the contribution of terms $C_{OO}(x = \text{NN sites}) = -\langle \theta_O \rangle^2$).

From Eq. (A2) for $J \neq K$, the lead $x = O$ term on the RHS of $-\langle \theta_{CO} \rangle \langle \theta_O \rangle$ is negative (as distinct species cannot occupy the same site) facilitating anticorrelation in coverage fluctuations. See Sec. III.B.

Finally, we note that in our ''hybrid'' model where CO (ads) is randomly distributed on non-O (ads) sites, one has $C_{COCO}(x \neq O) = \langle \theta_{CO} \rangle^{-2} (1 - \langle \theta_O \rangle)^{-2} \, C_{OO}(x)$ for an infinite system. This might suggest a simple connection between A_{CO} and A_O. However, this is not the case, as this relation between spatial correlations is not satisfied for a finite system. To see why this relation fails, consider the simplest case where $N_O = 0$, so $C_{OO} = 0$. Then, if N_{CO} fluctuates in time between the extreme values of $N_{CO} \approx 0$ and $N_{CO} \approx L^2$, it follows that $C_{COCO} > 0$ upon taking a temporal average $\langle \rangle$.

APPENDIX B: RATE W_{O2ads} (TABLE I) IN THE POPULATION DYNAMICS FORMULATION

A nontrivial challenge (even for an infinite system) is to suitably approximate P_8, the probability of finding an ensemble of eight non-O (ads) sites (hereafter denoted as **Z** sites). Figure 14(a) indicates a natural factorization[40] of the form $P_8 = Q_7 Q_6 \ldots Q_1 P(\mathbf{Z})$. Here, Q_j is the conditional probability to find a **Z** site adjacent to a specified cluster of j other **Z** sites (where such specified sites are indicated by italic Z's in Fig. 14). Also, $P(\mathbf{Z}) = (L^2 - N_O)/L^2$ is the probability of finding a **Z** site. For all cases except $j = 3$, there is just one nearest-neighbor site in the specified cluster. Then, for an infinite system, in the pair (Kirkwood) approximation that accounts only for the influence of this closest site in the specified cluster, one would set $Q_j \approx Q(\mathbf{Z}Z)[\equiv Q(\text{pair})] = P_{ZZ}/P_Z = (1 - 2\theta_O)/(1 - \theta_O)$.[35,40] For a finite system, we use

$$Q_j \approx [L^2 - (j-1) - 2N_O]/[L^2 - (j-1) - N_O] \equiv Q_j(\text{pair}). \tag{B1}$$

This expression accounts for the feature that in considering the probability of finding a **Z** site given one neighboring **Z**, we regard the N_O adsorbed O species as distributed on $L^2 - (j-1)$ sites, since for Q_j one knows that $j-1$ other sites are specified as in state **Z**. Analysis of Q_3 is complicated by the fact that the **Z** site of interest has two neighboring sites in the specified cluster. We choose the factorization indicated in Fig. 14(b) yielding $Q_3 \approx Q(\text{pair})^2/P(\mathbf{Z})$ for an infinite system.[35] For the finite system, we use $Q_3 \approx Q_3$ (pair) Q_2 (pair) $L^2/(L^2 - 1 - N_O)$.

[1] R. I. Masel, *Principles of Adsorption and Reaction on Solid Surfaces* (Wiley-Interscience, New York, 1996).

[2] C. R. Henry, Surf. Sci. Rep. **31**, 231 (1998).

[3] M. F. H. van Tol, A. Gielbert, and B. E. Nieuwenhuys, Catal. Lett. **16**, 297 (1992).

[4] V. Gorodetskii, W. Drachsel, and J. H. Block, Catal. Lett. **19**, 223 (1993).

[5] V. Gorodetskii, J. Lauterbach, H.-H. Rotermund, J. H. Block, and G. Ertl, Nature (London) **370**, 276 (1994).

[6] Yu. Suchorski, R. Imbihl, and V. K. Medvedev, Surf. Sci. **401**, 392 (1998).

[7] Yu. Suchorski, J. Beben, and R. Imbihl, Surf. Sci. Lett. **405**, L477 (1998).

[8] Yu. Suchorski, J. Beben, and R. Imbihl, Prog. Surf. Sci. **59**, 343 (1998).

[9] Yu. Suchorski, J. Beben, E. W. James, J. W. Evans, and R. Imbihl, Phys. Rev. Lett. **82**, 1907 (1999).

[10] K. Fichthorn, E. Gulari, and R. M. Ziff, Phys. Rev. Lett. **63**, 1527 (1989).

[11] V. K. Medvedev, Yu. Suchorski, and J. H. Block, Vacuum **46**, 563 (1995).

[12] Yu. Suchorski, J. Beben, and R. Imbihl, Ultramicroscopy **73**, 67 (1998).

[13] E. W. Müller and T. T. Tsong, *Field Ion Microscopy* (American Elsevier, New York, 1969).

[14] G. Ertl, Surf. Sci. **299/300**, 742 (1994).

[15] R. Imbihl and G. Ertl, Chem. Rev. **95**, 697 (1995).

[16] Yu. Suchorski, W. A. Schmidt, N. Ernst, J. H. Block, and H. J. Kreuzer, Prog. Surf. Sci. **48**, 121 (1995).

[17] W. A. Schmidt, Yu. Suchorski, J. H. Block, H. J. Kreuzer, and R. L. C. Wang, Surf. Sci. **326**, 243 (1995).

[18] J. T. Yates, Jr., J. Vac. Sci. Technol. A **13**, 1359 (1995).

[19] T. Zambelli, J. Winterling, J. Trost, and G. Ertl, Science **273**, 1688 (1996).

[20] B. Rausenberger, W. Swiech, C. S. Rastomjee, M. Mundschau, W. Engel, E. Zeitler, and A. M. Bradshaw, Chem. Phys. Lett. **215**, 109 (1993); M. Tammaro, J. W. Evans, C. S. Rastomjee, W. Swiech, A. M. Bradshaw, and R. Imbihl, Surf. Sci. **407**, 162 (1998).

[21] Yu. Suchorski, J. Beben, and R. Imbihl, Surf. Sci. **454–456**, 331 (2000).

[22] N. Aubry, P. Holmes, J. L. Lumley, and E. J. Stone, J. Fluid Mech. **192**, 115 (1988).

[23] L. Sirovich, Phys. Rev. Lett. **65**, 1356 (1990).

[24] J. J. Binney, N. J. Dowrick, A. J. Fisher, and M. E. J. Newman, *The Theory of Critical Phenomena: An Introduction to the Renormalization Group* (Clarendon, Oxford, 1992); C. Domb, *The Critical Point* (Taylor & Francis, London, 1996).

[25] W. Horsthemke and R. Lefever, *Noise-Induced Transitions* (Springer, Berlin, 1984); P. Hänggi, P. Talkner, and M. Borkovec, Rev. Mod. Phys. **62**, 251 (1990).

[26] A. S. Mikhailov and A. Yu. Loskutov, *Foundations of Synerget-*

ics II, 2nd ed. (Springer, Berlin, 1996).
[27] M. O. Vlad and J. Ross, J. Chem. Phys. **100**, 7268 (1994); A. S. Mikhailov, Phys. Lett. **73A**, 143 (1979); Z. Phys. B: Condens. Matter **41**, 277 (1981).
[28] J. W. Evans and T. R. Ray, Phys. Rev. E **50**, 4302 (1994).
[29] M. Tammaro and J. W. Evans, J. Chem. Phys. **108**, 762 (1998); **103**, 10 277 (1995).
[30] W. H. Weinberg, Annu. Rev. Phys. Chem. **34**, 217 (1983).
[31] R. M. Ziff, E. Gulari, and Y. Barshad, Phys. Rev. Lett. **56**, 2553 (1986).
[32] C. R. Brundle, R. J. Behm, and J. A. Barker, J. Vac. Sci. Technol. A **2**, 1038 (1984); S.-L. Chang and P. A. Thiel, Phys. Rev. Lett. **59**, 296 (1987).
[33] R. J. Behm, P. A. Thiel, P. R. Norton, and G. Ertl, J. Chem. Phys. **78**, 7437 (1983).
[34] V. P. Zhdanov and B. Kasemo, Surf. Sci. **412/413**, 527 (1998).
[35] E. W. James, S. Song, and J. W. Evans, J. Chem. Phys. **111**, 6579 (1999).
[36] D.-J. Liu and J. W. Evans, Phys. Rev. Lett. **84**, 955 (2000).
[37] M. Xu, J. Liu, and F. Zaera, J. Chem. Phys. **104**, 8825 (1996).
[38] For mean-field reaction-diffusion systems with Laplacian diffusion, this equistability criteria can often be reformulated in terms of Lypanov functions, e.g., N. F. Hansen and J. Ross, J. Phys. Chem. **100**, 8040 (1996); F. Schloegl, Z. Phys. **253**, 147 (1972). For LG models, this equistability is controlled by the nontrivial nature of chemical diffusion in the mixed reactant adlayer (Refs. 29,36).
[39] D. A. McQuarrie, Adv. Chem. Phys. **15**, 149 (1970); H. Malchow and L. Schimansky-Geier, *Noise and Diffusion in Bistable Nonequilibrium Systems* (Teubner, Berlin, 1985); D. Considine, S. Redner, and H. Takayasu, Phys. Rev. Lett. **63**, 2857 (1989).
[40] J. W. Evans, Rev. Mod. Phys. **65**, 1281 (1993).